Supplementary Information

Intervalence plasmons in boron-doped diamond

Souvik Bhattacharya,[1] Jonathan Boyd,[2] Sven Reichardt,[3], Valentin Allard,[4] Amir Hossein Talebi,[3] Nicolò Maccaferri,[5] Olga Shenderova,[6] Aude L. Lereu,[4] Ludger Wirtz,[3] Giuseppe Strangi,[2,7] and R. Mohan Sankaran[1]

[1]Department of Nuclear, Plasma, and Radiological Engineering, The Grainger College of Engineering, University of Illinois Urbana-Champaign, Champaign, IL, U.S.A.

[2]Department of Physics, Case Western Reserve University, Cleveland, OH, U.S.A.

[3]Department of Physics and Materials Science, University of Luxembourg, Luxembourg

[4]Aix Marseille Univ, CNRS, Centrale Med, Institut Fresnel, Marseille, France

[5]Department of Physics, Umeå University, Sweden

[6]Adamas Nanotechnologies, Raleigh, NC, U.S.A.

[7]NLHT Labs, Department of Physics, University of Calabria, Rende, Italy

Supplementary Note 1. Characterization of diamond samples by transmission electron microscopy. Optical images of suspensions of BDD and undoped diamond crystals in ethanol are shown in Supplementary Fig. 1. The presence of boron is manifested visibly by the bluish appearance of the BDD suspension. Supplementary Figs. 2a and 2b show high-resolution transmission electron microscopy (HR-TEM) images of the BDD and undoped diamond samples, respectively. The samples were found to consist of nearly identically-sized particles on the order of ~1 μm (inset, Supplementary Figs. 1a and 1b). The lattice fringes confirm the crystalline nature of these particles. We note that despite the addition of boron, there is no observable loss of crystallinity in the boron-doped samples. Moreover, to preserve the crystallinity of these microdiamonds, no special TEM sample preparation or post-treatment was performed on either sample.

Supplementary Fig. 1c shows the core-loss region of the electron energy loss (EEL) spectra obtained from BDD and undoped diamond, respectively. We observe a sharp peak ca. 292 eV for both samples, which is ascribed to σ* transitions corresponding to sp^3-hybridized carbon atoms indicative of crystalline diamond, and a smaller peak at ca. 284 eV, which is ascribed to π* transitions corresponding to sp^2-hybridized carbon atoms indicative of graphitic carbon. The π* peak is small compared to the σ* peak, confirming a high sp^3/sp^2 ratio in these samples. Despite the stark contrast in color of these samples, we did not observe a B K-edge signal in the core-EELS region which would have occurred from ca. 190 eV to ca. 240 eV.[1]

In order to try to observe the B K-edge, which would allow us to co-locally study the variation of VEELS with the presence of boron, we analyzed the core EELS spectra further by integrating over different areas to accumulate the signal (see Supplementary Fig. 3). In all cases, no B K edge signal was observed. The lack of a signal is consistent with the boron concentration in our samples, which is <1000 ppm (see Supplementary Note 2), being below the detection limit of core-EELS generally at or above a few at. %.[1,2]

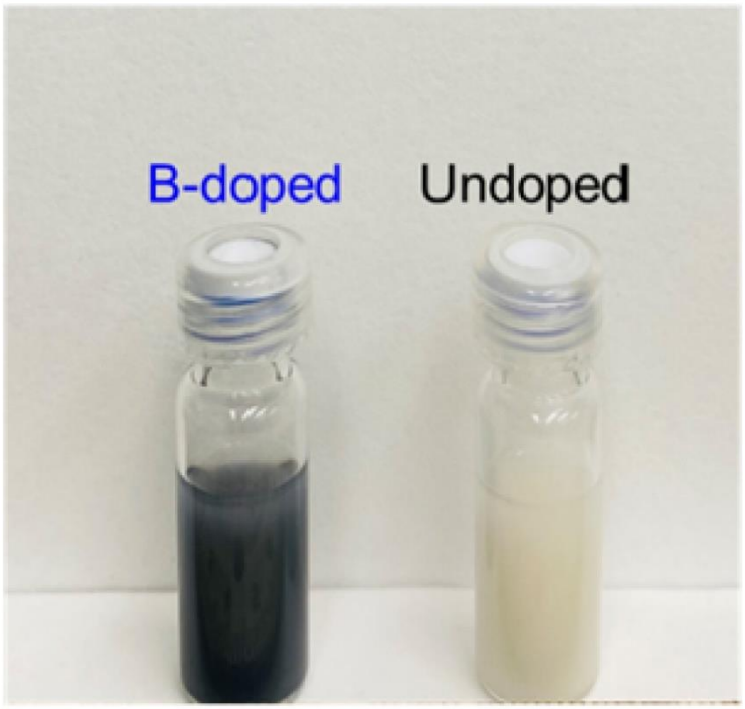

Supplementary Fig. 1: Photographs of diamond samples used in this work

Photographs of BDD (left) and undoped diamond (right) crystals synthesized using high-pressure high-temperature (HPHT) dispersed in ethanol. The BDD sample appears deep blue due to the presence of the boron dopant.

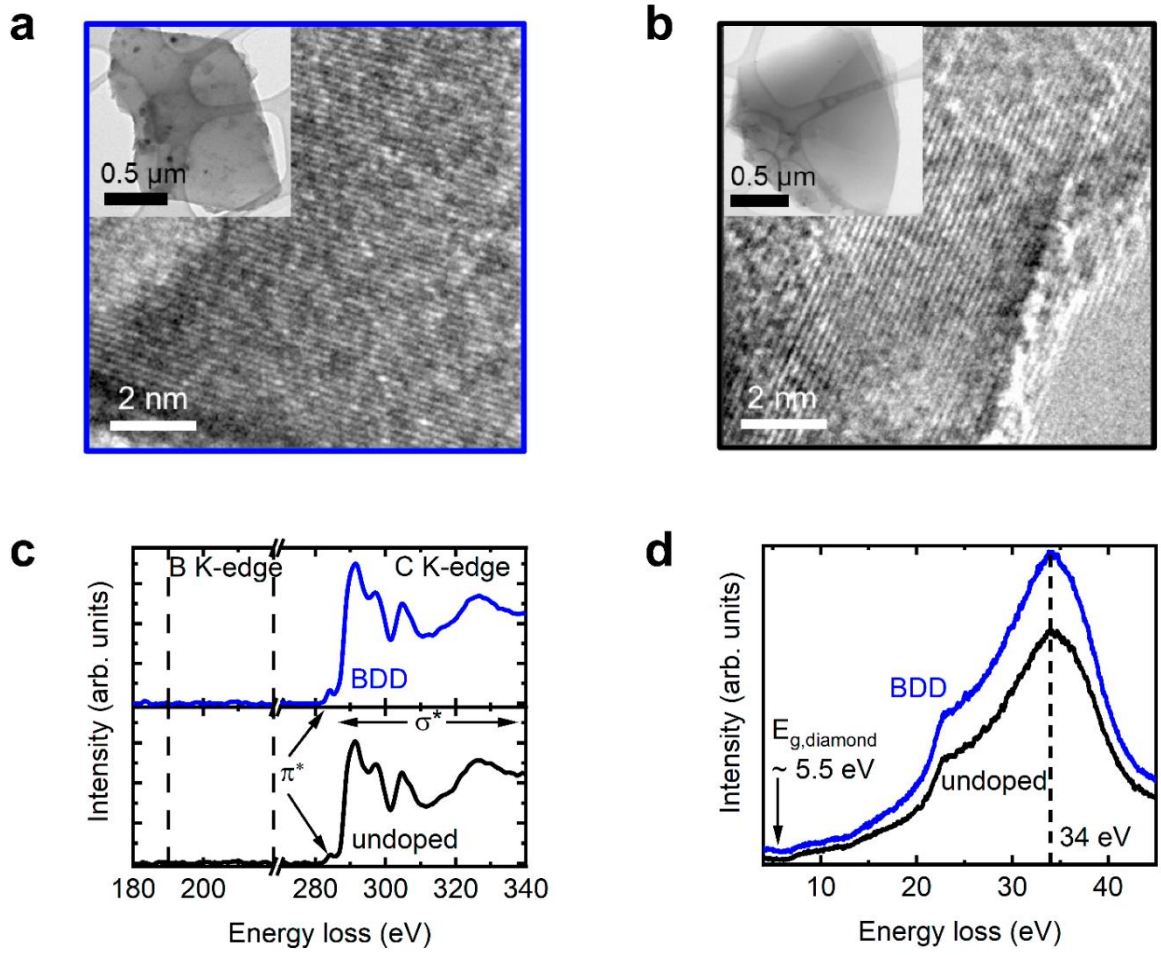

Supplementary Fig. 2: Characterization of BDD and undoped diamond samples

a-b, Representative HRTEM images of BDD, **(a)** and undoped diamond, **(b)** particles showing lattice fringes. The insets show that the diamond samples consist of identically sized particles. **c**, Core-EELS spectra acquired from BDD and undoped diamond samples. While a clear C K-edge signal was observed in both samples showing a high sp^3/sp^2 ratio, no B K-edge signal was observed from the BDD sample. **d**, EELS spectra acquired from BDD and undoped diamond showing the volume plasmon resonance at ca. 34 eV, proportional to the valence electron density of diamond. The onset of this signal occurs at ca. 5.5 eV which coincides with the bandgap of diamond.

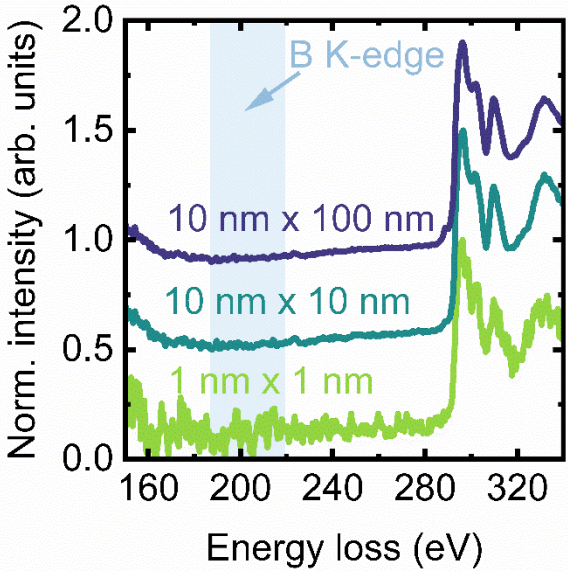

Supplementary Fig. 3: Core-loss EELS analysis of the B K-edge signal

Core-loss STEM-EEL spectra of BDD collected with 1 nm x 1 nm spatial resolution and integrated over different areas. The spectra were corrected for background by a power law fit. The absence of a discernable B K-edge signal in all cases is due to the boron concentration being below the detection limit of EELS.

Supplementary Note 2. Modeling the Fano lineshape measured in the micro Raman spectra of BDD to estimate the average free charge carrier concentration. The average hole density in BDD was estimated by analysis of the Fano interference observed in micro Raman spectra of semiconductor materials, which occurs as a result of the interaction of phonons with a continuum of electronic excitations such as those opened up by hole doping in BDD. This method is non-destructive and sensitive to dopant concentrations down to 100 ppm.[3] The comprehensive overall procedure developed by Mortet et al. was used to model the asymmetric line shape by a combination of two discrete excitations, the zone-center phonon (ZCP) and the phonon-density-of-states (PDoS) maximum, and a continuum termed as the electronic Raman scattering (ERS) background, the latter of which is a direct consequence of the holes created by the introduction of boron.[4] The model was fit to the experimentally-obtained spectra using least squares regression (R^2=0.968), and the converged values of the fit parameters such as the spectral position shifts and FWHMs of the Fano-modified ZCP (1327 cm^{-1}), and the PDoS maximum (1295 cm^{-1}), were found to correspond to a boron doping level below the semiconductor-metal transition ($[B] \leq 4 \times 10^{20}$ cm^{-3}). The parameter of interest in this framework is the asymmetry coefficient, q, which is defined as the ratio of the transition probability of the discrete excitation to that of the continuum excitations, and whose converged absolute value is inversely correlated with the charge carrier density.[5,6] By comparing q_{ZCP} (= -164) and q_{PDoS} (= -0.41) obtained from our analysis with reported values measured by Hall measurements of crystalline BDD films,[4] we estimated the average hole density of our BDD sample to be $\sim 5 \times 10^{19}$ cm^{-3}. It is noteworthy that this value is an average over several BDD particles and does not account for doping inhomogeneity across individual BDD particles.

Supplementary Note 3. Tip-enhanced Raman Spectroscopy (TERS) to probe the spatial variation of boron doping at the nanoscale. As detailed in Supplementary Note 2, micro Raman characterization of BDD shows a Fano resonance that can be modeled to obtain the boron concentration. However, because the laser spot size in micro Raman spectroscopy is ~10 μm and the particles are ~100s of nm in size, the boron concentration that is obtained is an average over multiple particles. To obtain the boron concentration with smaller spatial resolution, we performed TERS. In TERS, nanometer scale resolution is possible with the main limitation being sufficient signal. Supplementary Fig. 4 shows TER spectra collected from a representative BDD particle over 3 different scales: ~1 μm, 400 nm, and 200 nm, respectively. As the spatial area decreases, the Fano-type lineshape becomes more difficult to observe and below 200 nm was not clear. Nonetheless, we were able to improve the spatial resolution as compared to micro Raman and map single particles. The TER spectra were modeled by the same procedure discussed previously (see Supplementary Note 2). At 1 μm, the asymmetry factor of the PDoS contribution (q_{PDoS}) obtained post-modeling (R^2 = 0.947) was found to be -1.15 while q_{ZCP} was a large negative value (Supplementary Fig. 4a). The boron doping level for these parameter values corresponds to roughly ~800 ppm based on similar modeling in literature, which represents an average over a single particle and is very close to the doping level obtained by micro Raman spectroscopy.[4] Starting at 400 nm, variations were observed from different regions (Supplementary Fig. 4b). The q_{PDoS} from two regions were found to be -2.3 and 0.2, respectively, while q_{ZCP} were large negative values (R^2 = 0.956 and 0.937, respectively), corresponding to boron doping levels of ~200-400 ppm and ~1000 ppm, respectively. For 200 nm (Supplementary Fig. 4c), the q_{PDoS} from two regions (2 and 3) were calculated to be roughly similar at ~0.4 (R^2 = 0.965 and 0.951 respectively), corresponding to a boron doping level of ~200-400 ppm, and two regions (1 and 4) were below the limit of fitting the Fano-line-shape and therefore, less than ~200 ppm. Overall, TERS confirms that the boron concentration varies within single particles over a relatively wide range, from less than 200 ppm to ~1000 ppm.

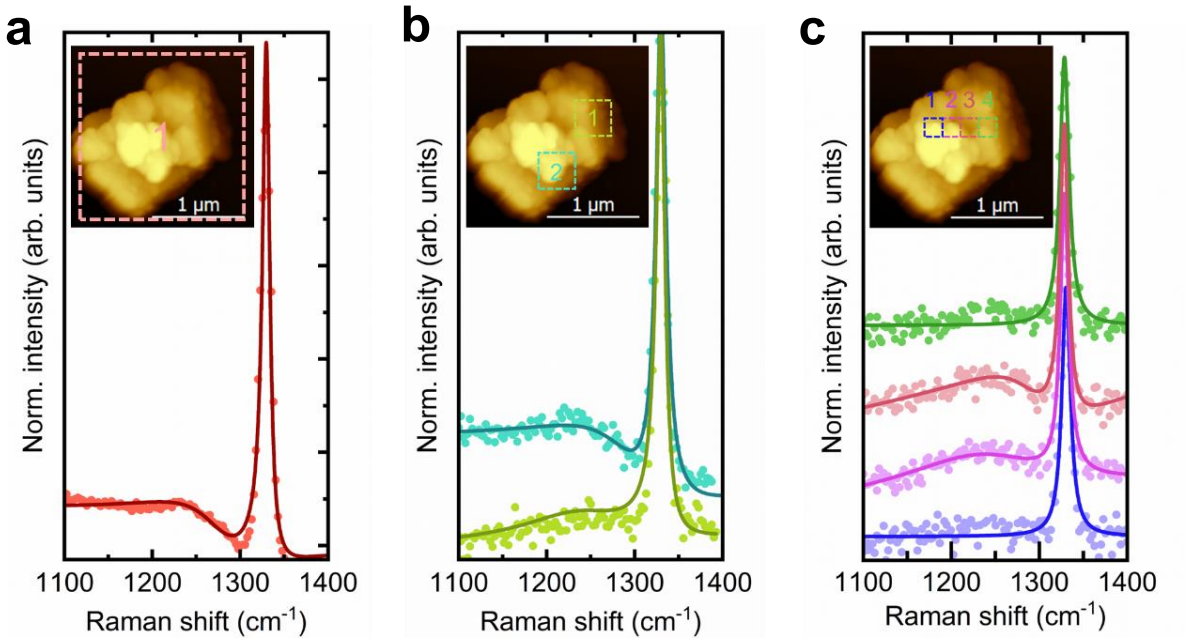

Supplementary Fig. 4: TERS characterization and analysis of BDD

Experimental TER spectra (scatter points) and corresponding model fits of the Fano lineshape (solid line) for a representative BDD particle at spatial resolutions of **a**,1 µm. **b**, 400 nm, and **c**, 200 nm. For 400 and 200 nm, TER spectra were collected from different regions of the particle. Inset shows an AFM image of the BDD particle and locations corresponding to TER spectra. Variation of the Fano-type lineshape indicates heterogeneity of boron doping within a single particle.

Supplementary Note 4. Isolation and analysis of inelastic VEELS signal from BDD and undoped diamond particles. Methods to fit and subtract the elastic ZLP component in order to isolate the inelastic component from raw VEEL spectra remain challenging and are an active area of research.[7,8] As shown in Supplementary Fig. 5, two different methods were used here to analyze the inelastic VEEL signal. In the first method, which we term the 'spectral fitting' method, the ZLP was modeled by a vacuum VEEL spectrum, and the inelastic signal was fit to a Voigt function to generally account for any Gaussian and Lorentzian contributions (see Supplementary Fig. 5c and 5d). To independently confirm this approach, a more conventional procedure to separate the inelastic signal by subtracting the ZLP from VEEL spectra was also explored (see Supplementary Fig. 5e and 5f).[8] Both methods produced identical spectral position and overall shape of the inelastic signal. However, the subtraction method produced non-physical features such as negative signals. Therefore, the fitting method was chosen for analysis of all VEEL spectra. Supplementary Figs. 6 and 7 show VEELS spectra obtained from BDD and undoped diamond samples, respectively, where the inelastic VEEL signal unique to BDD manifests itself as a shoulder or asymmetry on the zero-loss peak (ZLP).

The spatial variation of the inelastic signal across particle areas was studied by collecting spectra at each 1 nm x 1 nm pixel of the STEM images and applying the same fitting method. Color maps were constructed for different spectral energies by integrating the inelastic VEEL signal within a narrow energy slice centered around the energy value of interest. Color maps corresponding to 0 eV accounted for the attenuation of the ZLP resulting from variation in the thickness of the sample. The intensities were normalized by subtracting this contribution of the sample thickness in order to only show variation from inelastic electron scattering processes (Supplementary Figs. 9 and 11).

We further analyzed the variation of the inelastic VEELS signal with thickness by quantifying the thickness of the particles using a previously reported log-ratio method.[9] Assuming an inelastic mean free path of 150 nm for 150 keV electrons in diamond[10], the calculations show that the thinnest regions near the edge of the particles correspond to ~2-3 nm in thickness, while the thicker regions into the body of the particles correspond to ~15-20 nm in thickness. Despite this relatively large variation in thickness, the measured inelastic VEEL signal at ca. 0.15 eV shows a weak correlation, indicating that the signal is largely independent of the sample thickness.

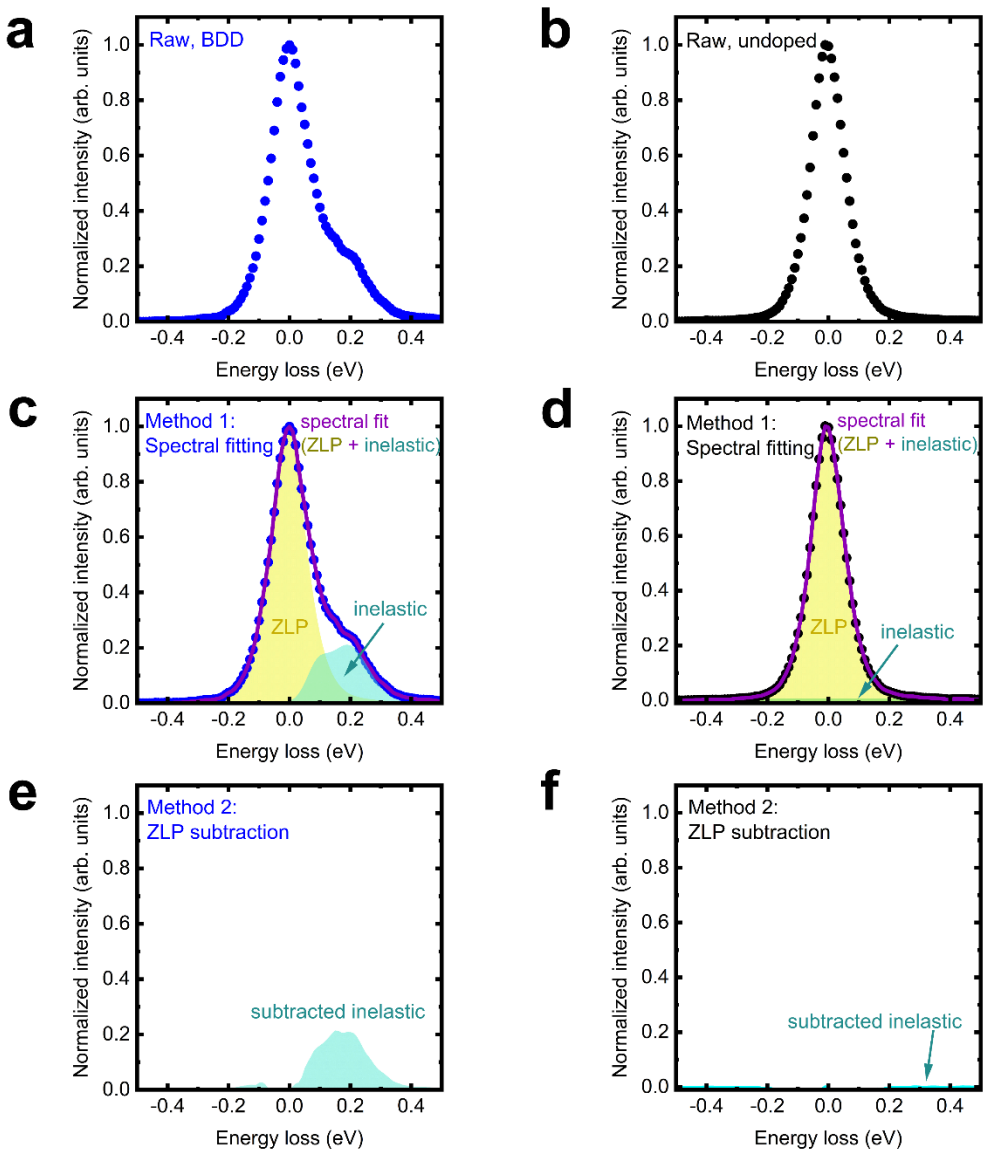

Supplementary Fig. 5: Isolation and analysis of the inelastic component of VEEL spectra

Analysis of VEEL spectra collected from **a,** BDD and **b,** undoped diamond by two methods: **c, d,** spectral fitting, and **e, f,** ZLP subtraction. Both methods independently confirm identical inelastic VEEL signatures present only in BDD.

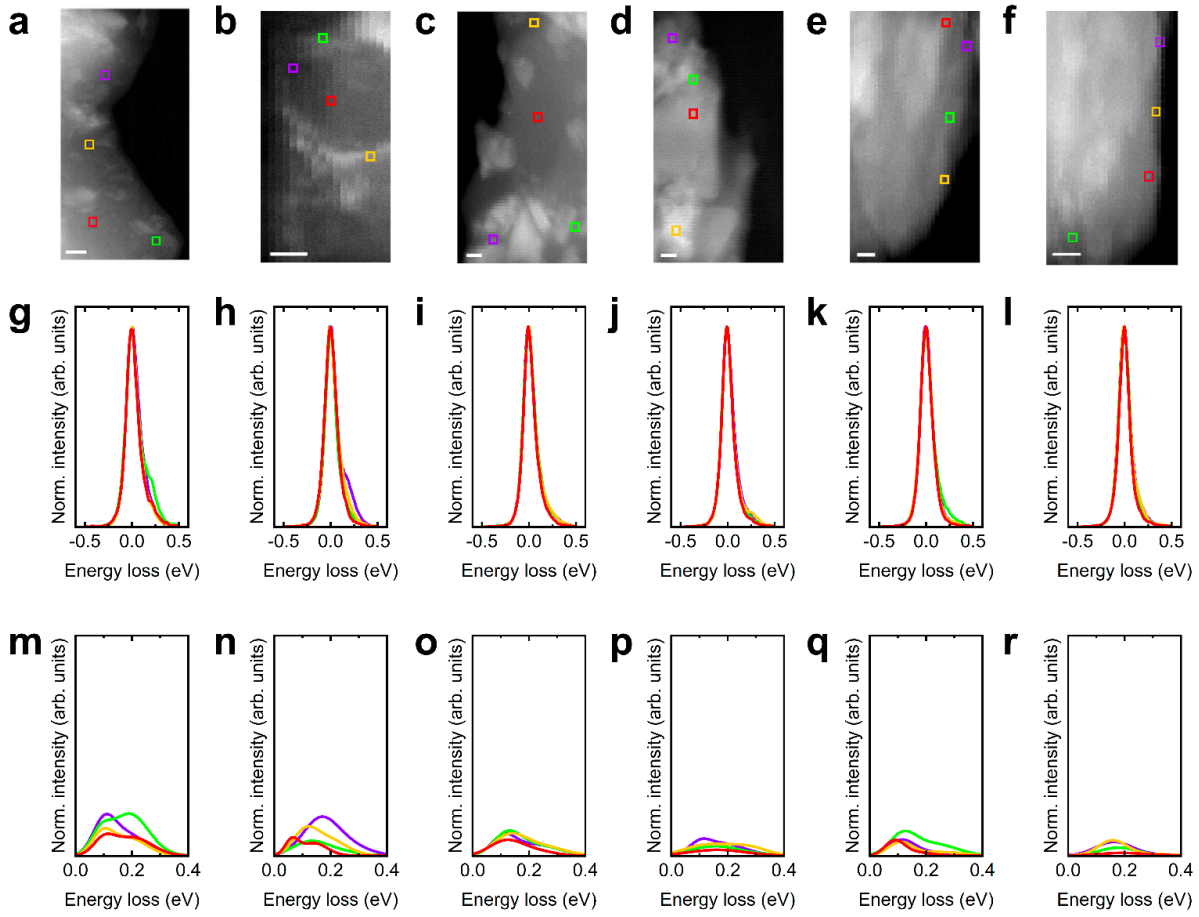

Supplementary Fig. 6: Experimental VEEL spectral analysis of different BDD particles

a-f, Annular dark field (ADF) images of sections of different BDD particles. All scale bars correspond to 10 nm. **g-l**, Raw VEEL spectra taken at 4 1 nm x 1 nm spots from each BDD particle shown in (a)-(f). **m-r**, Residual inelastic VEEL signal isolated after separation from the ZLP from the raw spectra shown in (g)-(l).

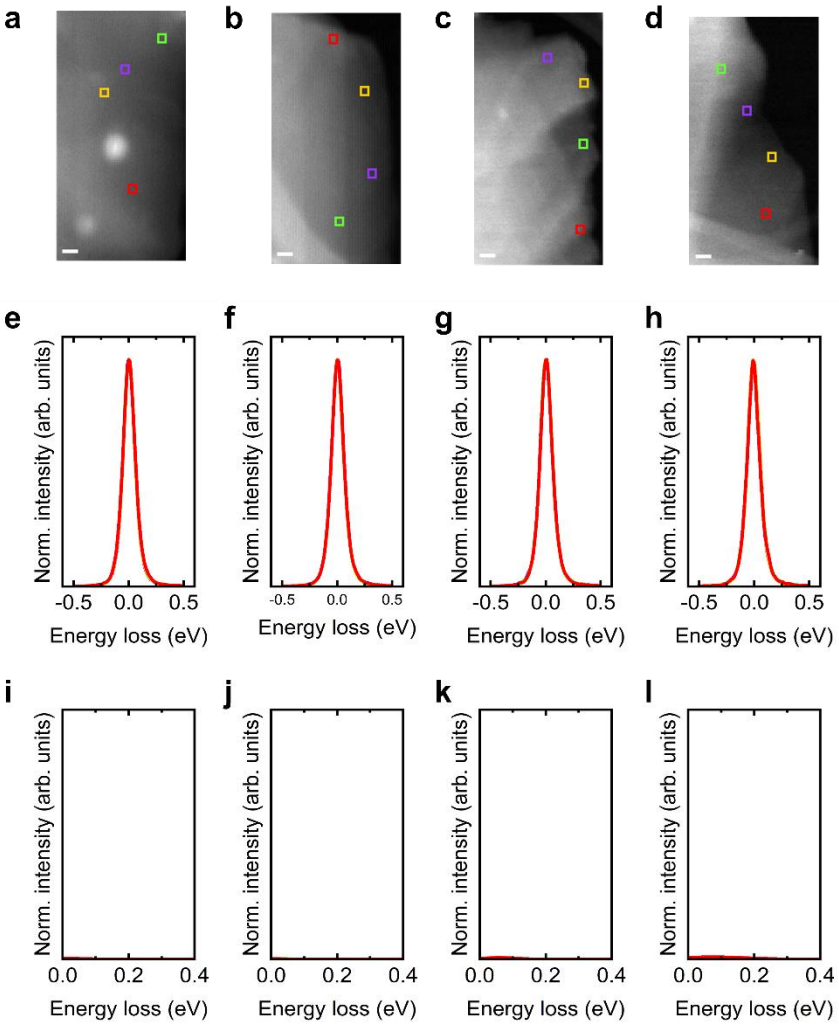

Supplementary Fig. 7: Experimental VEEL spectral analysis of different undoped diamond particles

a-d, Annular dark field (ADF) images of sections of different undoped diamond particles. All scale bars correspond to 10 nm. **e-h**, Raw VEEL spectra taken at 4 1 nm x 1 nm spots from each undoped diamond particle shown in (a)-(d). **i-l**, Residual inelastic VEEL signal isolated after separation from the ZLP from the raw spectra shown in (e)-(h).

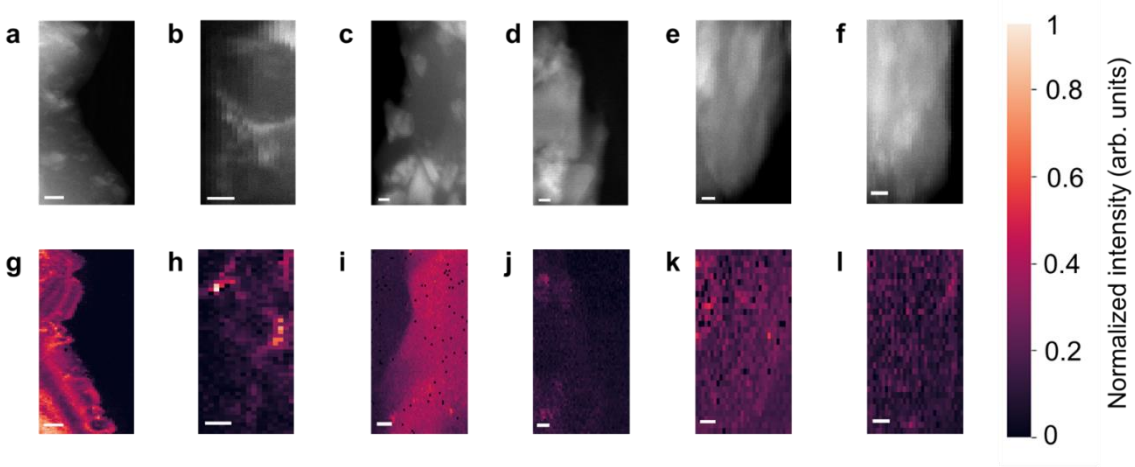

Supplementary Fig. 8: VEELS intensity color maps for BDD

a-f, Annular dark field (ADF) images of different BDD particles. **g-l**, Color maps showing spatial variation of the normalized inelastic VEEL signal at 0.15 eV energy for each particle shown in (a)-(f). All scale bars correspond to 10 nm and the color bar corresponds to the normalized inelastic VEEL intensity on a scale of 0 to 1 in arbitrary units.

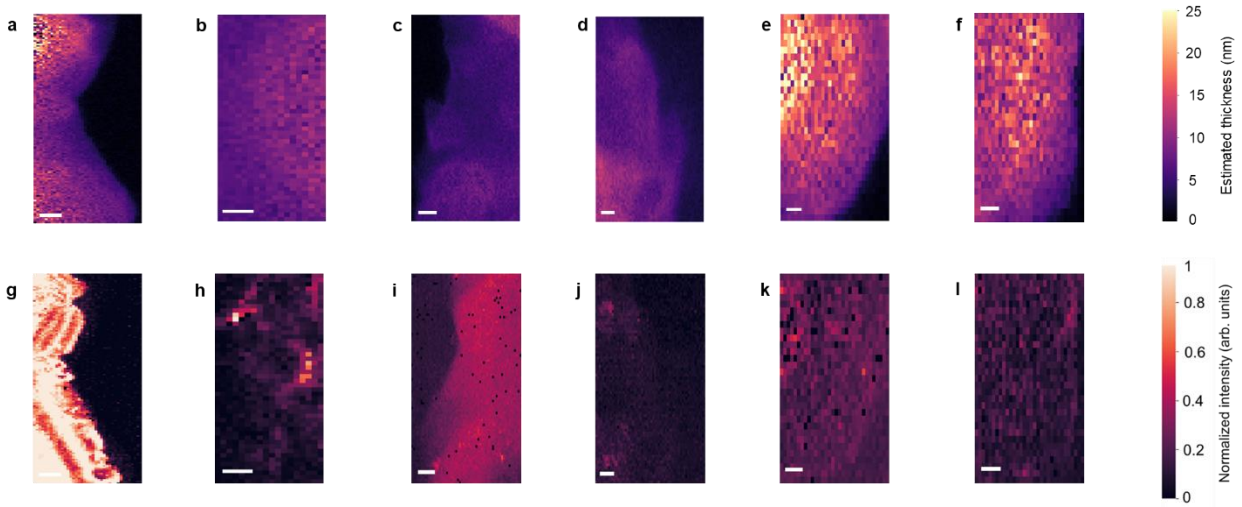

Supplementary Fig. 9: VEELS intensity correlation with sample thickness

a-f, False color maps showing the variation in particle thickness calculated by the log-ratio method for different BDD particles assuming an inelastic mean free path of 150 nm for 300 keV electrons. **g-l**, Color maps showing spatial variation of the normalized inelastic VEEL signal at 0.15 eV energy for each particle shown in (a)-(f). All scale bars correspond to 10 nm and the color bar corresponds to the normalized inelastic VEEL intensity on a scale of 0 to 1 in arbitrary units.

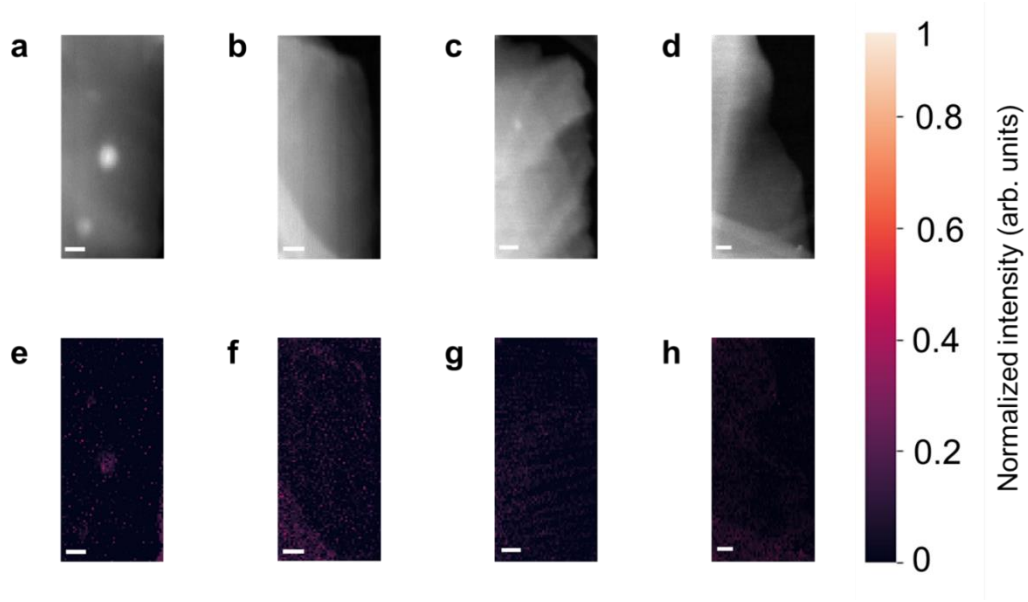

Supplementary Fig. 10: VEELS intensity color maps for undoped diamond

a-d, Annular dark field (ADF) images of different undoped diamond particles. **e-h**, Color maps showing spatial variation of the normalized inelastic VEEL signal at 0.15 eV energy for each particle shown in (a)-(d). All scale bars correspond to 10 nm and the color bar corresponds to the normalized inelastic VEEL intensity on a scale of 0 to 1 in arbitrary units.

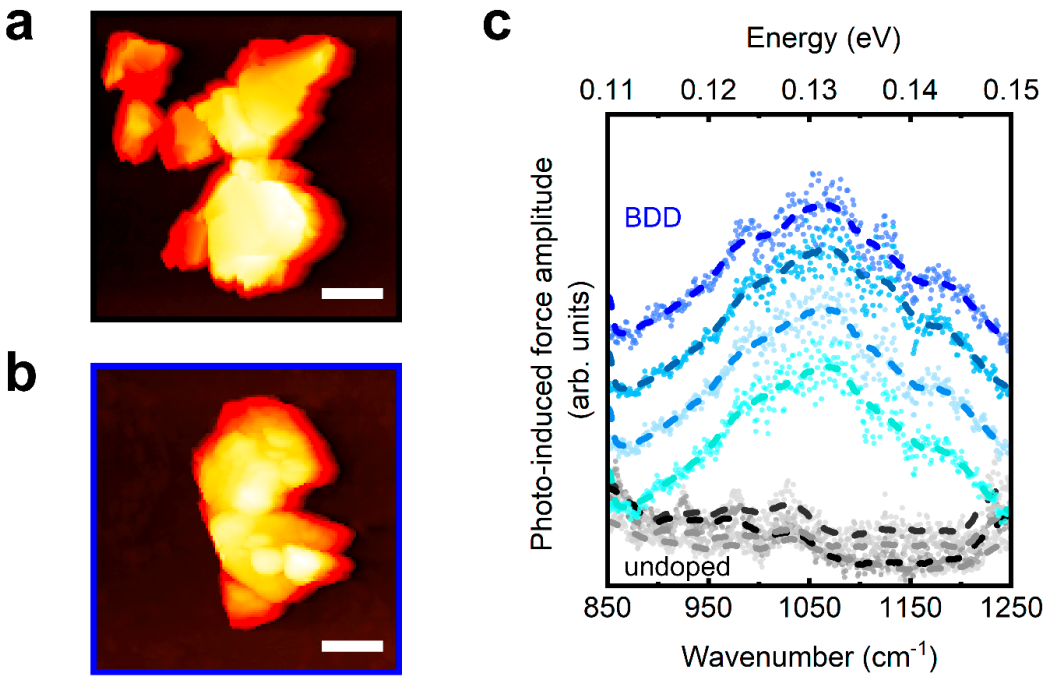

Supplementary Fig. 11: Photo-induced force microscopy (PiFM) characterization of BDD and undoped diamond

a-b, Topographical scans of representative undoped diamond (a) and BDD (b) particles. The scale bar represents 1 μm. **c**, PiFM spectra collected in the mid-IR regime from the undoped diamond (gray plots) and BDD (blue plots, offset for clarity) shown in (a) and (b). A peak around 0.13 eV is observed only for BDD which is correlated with absorbance.

Supplementary Note 5. s-SNOM analysis of BDD and undoped diamond. Scattering-Scanning Nearfield Optical Microscopy (s-SNOM) is a nanoscale characterization technique, conceptually similar to Photo-induced Force Microscopy (PiFM) but distinguished by its optical detection mechanism. Here, an incident electromagnetic field is focused beneath the tip of a metalized atomic force microscope (AFM) probe, thereby confining and localizing light-matter interactions at the nanoscale.[11] Through this interaction, s-SNOM generates spatially resolved images of both amplitude and phase shift of the scattered field, that is then demodulated at higher harmonics for proper optical nearfield interaction extraction.[12-14] In this study, s-SNOM scans were conducted by imaging BDD and undoped diamond crystals on a silicon substrate, with measurements taken at 1048 cm^{-1} (~ 0.13 eV) consistent with the resonance observed by VEELS and PiFM (see Methods for experimental details). Since the scattered field, E_s and the incident field, E_i are proportional *i.e.* $E_s \propto \sigma E_i$, the scattering coefficient σ can be used to obtain the sample's optical response to the incident excitation (phase and amplitude shift), The near field signal obtained from a normalization to a reference signal, obtained from the silicon substrate with quasi-uniform optical properties, in the infrared spectral range. The nearfield contrast η_n at the n^{th} demodulation harmonic is computed as[15]:

$$\eta_n = \frac{\sigma_n}{\sigma_{n,ref}} = \frac{a_n}{a_{n,ref}} e^{i(\varphi_n - \varphi_{n,ref})}$$

Where, η_n, σ_n and $\sigma_{n,ref}$ are complex quantities and a_n and φ_n are the optical amplitude and phase shifts induced by the interaction of the sample with the near-field infrared light. Given the optical properties of silicon[16] used in our experiments, the phase-shift of the reference area is set to 0 (light blue) and the amplitude to 1 (yellow) as shown in Fig. 4. Any changes in amplitude and phase are directly linked to variations in the optical near field interaction induced by the respective samples.

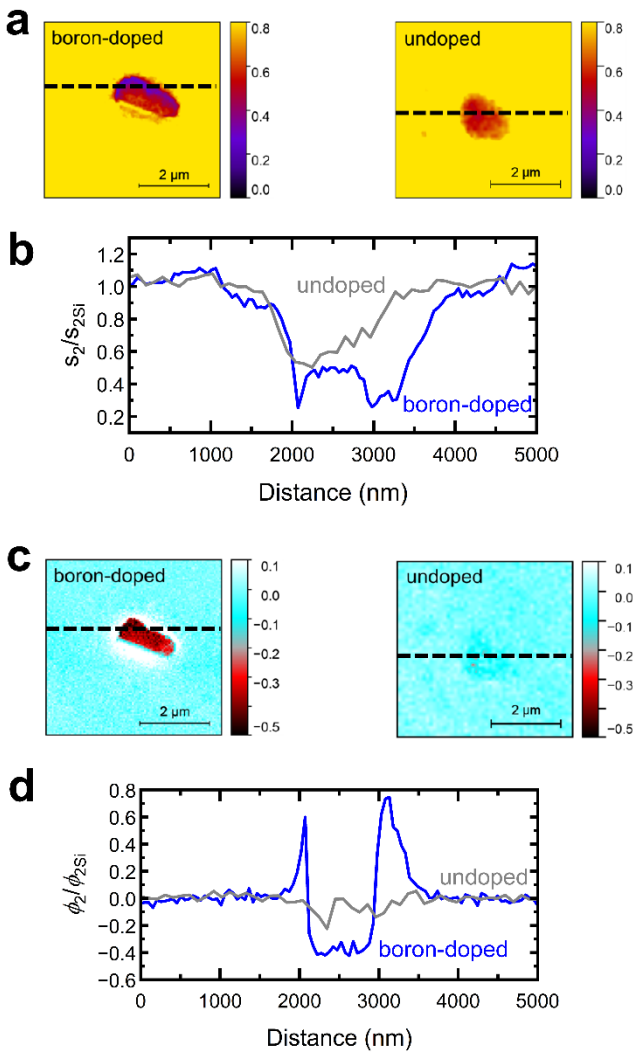

Supplementary Fig. 12: s-SNOM amplitude and phase profiles for BDD and undoped diamond.

a, Normalized amplitude images of BDD and undoped diamond as shown in Fig. 4. **b**, Profiles extract from (a) along the dashed lines showing similar variations in amplitude in BDD and undoped diamond. **c**, Normalized phase images of BDD and undoped diamond as shown in Fig. 4. **d**, Profiles extract from (b) along the dashed lines showing a phase contrast unique to BDD.

Supplementary Note 6. Thomas-Fermi model analysis of energy-loss function. A Drude-like model analysis of the energy-loss function was performed by applying the Thomas-Fermi model that has previously been used to predict infrared plasmons in heavily doped p-type and n-type silicon.[17] In this framework, the macroscopic dielectric permittivity of the material, $\varepsilon_M(\omega)$, is given by:

$$\varepsilon_M(\omega) = \varepsilon_0 \left(1 + \frac{i\omega_p^2 \tau}{\omega(1 - i\omega\tau)}\right)$$

where ε_0 is the relative static dielectric constant for diamond, ω_p is the plasma frequency, and τ is the collision time. The plasma frequency is further related to the hole density, n_H by:

$$\omega_p^2 = \frac{4\pi e^2 n_H}{\varepsilon_0 m^*}$$

where e denotes the elementary charge in Gauss units and m^* is the effective mass of the charge carrier, which are holes in the case of BDD, and is known to be dependent on contributions from both light holes (LH) and heavy holes (HH) in the valence band[18] The plasma frequency was calculated as a function of hole density using a single effective mass that accounts for contributions from the LH and HH bands[19], and further, by constructing the total macroscopic dielectric function, the energy-loss function was simulated for a range of hole densities (Supplementary Fig. 13).

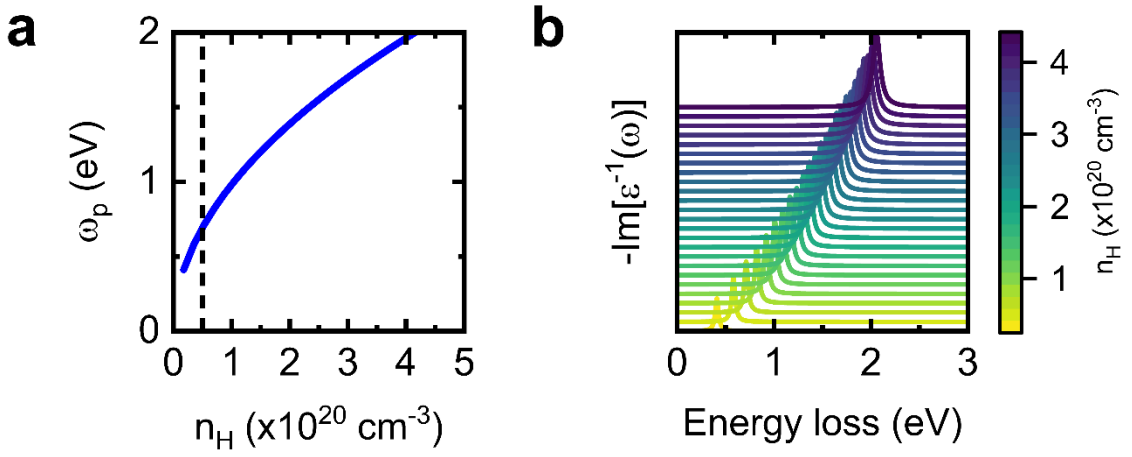

Supplementary Fig. 13: Thomas-Fermi model analysis of plasmonic behavior in BDD

a, Calculated plasma frequency, ω_p, as a function of hole density, n_H, in BDD. The dashed line corresponds to the average hole density of our BDD sample which according to this framework, predicts a plasma frequency at ca. 0.7 eV (Supplementary Note 5). **b,** Simulated loss spectra as a function of hole density.

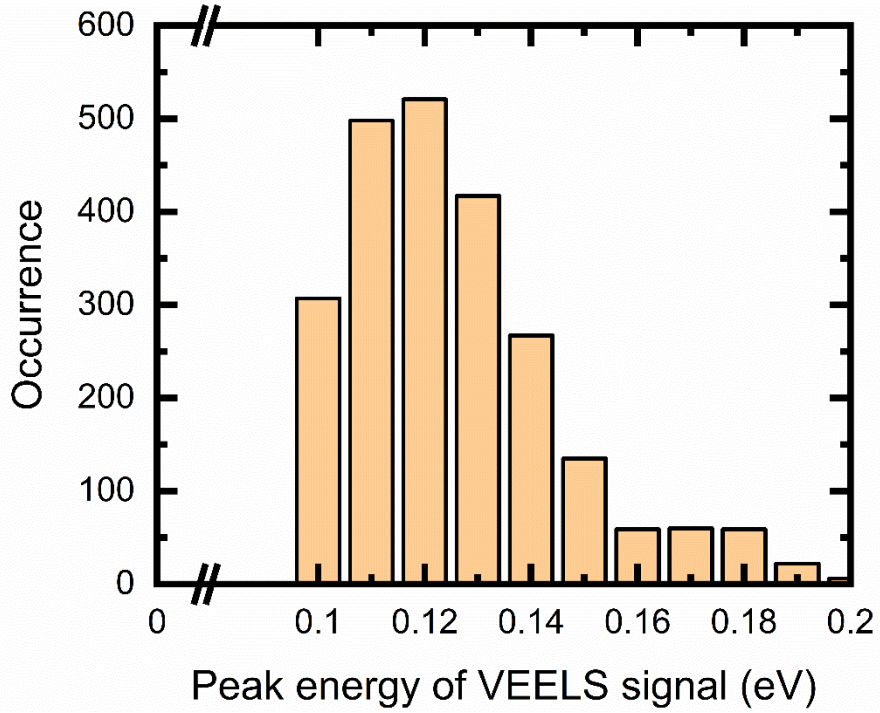

Supplementary Fig. 14: Histogram of VEELS peak energies

Statistical analysis of the peak energies measured by VEELS from 1 nm x 1 nm pixels over a 134 nm x 39 nm section of a representative BDD particle shown in Fig. 2c of the manuscript. The results show a distribution of energies between ~0.08 and 0.19 eV, with the highest occurrence at 0.12 eV.

Supplementary Note 7. Ab initio calculations of energy-loss function and absorption coefficient. First principles calculations of the energy-loss function, defined as $Im(-1/\varepsilon_M)$, and absorption coefficient, defined as $2\frac{\omega}{c}\ Im\left(\sqrt{\varepsilon_M(\omega)}\right)$, where ε_M is the total macroscopic dielectric function, were performed using ab initio methods following a three-step procedure: 1) defining an effective Fermi level as a function of the hole density, 2) relating the macroscopic dielectric function to the electronic transitions, and 3) constructing the total macroscopic dielectric function.

Effective Fermi level for BDD

The valence band structure of BDD was modeled by applying an effective Fermi level to the valence band structure of intrinsic diamond. The Fermi energy, ε_F, was calculated as a function of the hole density, n_H, by integrating the sum of the occupancies, $f_{\mathbf{k}n}$, of all electronic valence band states $|\mathbf{k}n\rangle$ over the first Brillouin zone (BZ):

$$8 - V_{UC}\, n_H = 2 \int_{BZ} \frac{d^3k}{V_{BZ}} \sum_{\substack{n \in Valence \\ bands}} f_{\mathbf{k}n}(\varepsilon_F)$$

where V_{UC} and V_{BZ} denote the volumes of the unit cell of diamond and the first BZ, respectively, the prefactor of two is related to the spin degeneracy of the bands, and at zero temperature the occupancies are given in terms of the Heaviside step function:

$$f_{\mathbf{k}n}(\varepsilon_F) = \Theta(\varepsilon_F - \varepsilon_{\mathbf{k}n}).$$

We note that the integral and sum on the right-hand side yield the total number of valence electrons per unit cell of diamond, which is equal to 8 for undoped diamond and is decreased by the number of holes in one unit cell, given by $V_{UC}\, n_H$. The equation above is a non-linear equation in ε_F, which we solve numerically using a golden section search. The calculation uses the experimentally-determined hole density and as such is independent of the exact energy level of the boron acceptor state, which could be modified by Coulomb interactions and is not easily captured in first-principles calculations.

Macroscopic dielectric function for BDD

On the level of non-interacting, single-particle transitions, the relation between the electronic transitions and their contribution to the macroscopic dielectric function is given by their independent-particle dielectric response function:

$$\varepsilon_M(\omega)|_{Valence}$$

$$= -\frac{16\pi e^2}{V_{UC}} \int_{BZ} \frac{d^3k}{V_{BZ}} \sum_{\substack{n,m \epsilon Valence \\ bands}} \left\{ [1 - f_{\mathbf{k}n}(\varepsilon_F)] f_{\mathbf{k}m}(\varepsilon_F) |\langle \mathbf{k}n|\hat{r}_x|\mathbf{k}m\rangle|^2 \frac{\varepsilon_{\mathbf{k}n} - \varepsilon_{\mathbf{k}m} + i\gamma}{(\hbar\omega)^2 - (\varepsilon_{\mathbf{k}n} - \varepsilon_{\mathbf{k}m} + i\gamma)^2} \right\}$$

where e is the elementary electronic charge in Gaussian units, V_{UC} denotes the volume of one unit cell of diamond, $\hat{r}_x$ is the x-component of the position operator (the y- and z-components yield the same result, due to the cubic symmetry of the crystal), and γ is a broadening constant that accounts for the finite lifetime of electronic transitions. The sum runs over all valence band combinations, n, m, but is constrained by the occupancy factors to pairs of occupied and unoccupied states, which for BDD were given by the Fermi energy shift. Since we consider the macroscopic dielectric function, only zero-momentum excitations, i.e., "vertical" electronic transitions, contribute.

Total macroscopic dielectric function

We also considered contributions of electronic transitions in intrinsic diamond to the macroscopic dielectric function of BDD, which stem from interband transitions between the valence and conduction bands. The total macroscopic dielectric function was then defined as:

$$\varepsilon_M(\omega) = \varepsilon_o + Re[\varepsilon_M|_{Valence}(\omega)] + i\ Im[\varepsilon_M|_{Valence}(\omega)]$$

where ε_o is the static dielectric constant of diamond. Since we focus on the low-frequency region <0.3 eV, which is much smaller than the band gap of diamond, the static approximation for the contribution of interband transitions is well-justified.

Direct calculation of intervalence plasmon properties

The frequency, ω_{pl}, and damping constant, γ_{pl}, of the intervalence plasmon can directly be obtained from the conditions:

$$Re\left[\varepsilon_M\left(\omega_{pl}\right)\right] = 0$$

and

$$\gamma_{pl} = \frac{2\ Im\left[\epsilon\left(\omega_{pl}\right)\right]}{\left.\frac{dRe[\varepsilon(\omega)]}{d\omega}\right|_{\omega=\omega_{pl}}},$$

with the latter expression obtained by a Taylor expansion of the real part of the dielectric function appearing in the denominator of the loss function. For the numerical evaluation of the derivative of the real part of the dielectric function at the plasmon frequency, we first convolved the real part of the dielectric function on a finite set of frequency points with a Savitzky-Golay filter to smoothen numerical artifacts related to the finite **k**-point sampling in the BZ integral appearing in the dielectric function.

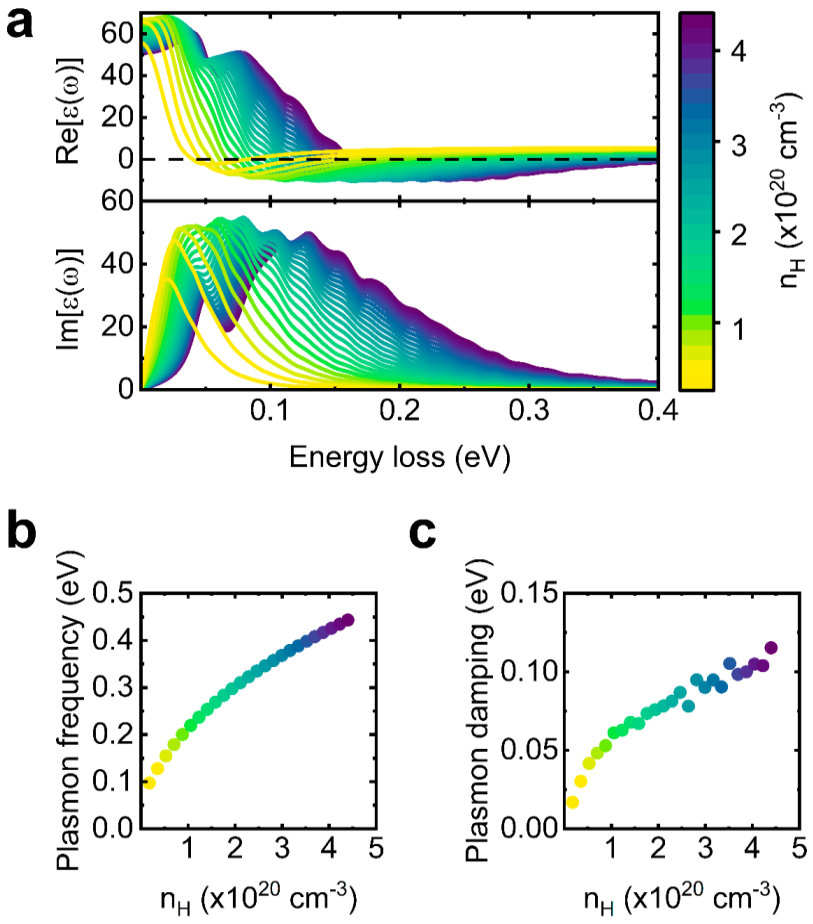

Supplementary Fig. 15: Spectral analysis of the ab-initio dielectric function for BDD

a, The real (top) and imaginary (bottom) parts of the simulated dielectric function for the different hole concentrations shown in Fig. 3. The real part exhibits a positive-to-negative crossover which meets the definition of a plasmon resonance. **b**, The intervalence plasmon frequency as a function of hole density shown in (a). **c,** The plasmon damping as a function of hole density, which is inversely related to the plasmon lifetime (Supplementary Note 5).

References

1 Heyer, S. *et al.* Toward Deep Blue Nano Hope Diamonds: Heavily Boron-Doped Diamond Nanoparticles. *ACS Nano* **8**, 5757-5764, doi:10.1021/nn500573x (2014).

2 Leapman, R. in *Transmission Electron Energy Loss Spectrometry in Materials Science and The EELS Atlas* 49-96 (2004).

3 Ashcheulov, P. *et al.* Conductivity of boron-doped polycrystalline diamond films: influence of specific boron defects. *The European Physical Journal B* **86**, 443, doi:10.1140/epjb/e2013-40528-x (2013).

4 Mortet, V. *et al.* New perspectives for heavily boron-doped diamond Raman spectrum analysis. *Carbon* **168**, 319-327, doi:https://doi.org/10.1016/j.carbon.2020.06.075 (2020).

5 Magidson, V. & Beserman, R. Fano-type interference in the Raman spectrum of photoexcited Si. *Physical Review B* **66**, 195206, doi:10.1103/PhysRevB.66.195206 (2002).

6 Becker, M., Gösele, U., Hofmann, A. & Christiansen, S. Highly p-doped regions in silicon solar cells quantitatively analyzed by small angle beveling and micro-Raman spectroscopy. *Journal of Applied Physics* **106**, 074515, doi:10.1063/1.3236571 (2009).

7 Koh, A. L. *et al.* Electron Energy-Loss Spectroscopy (EELS) of Surface Plasmons in Single Silver Nanoparticles and Dimers: Influence of Beam Damage and Mapping of Dark Modes. *ACS Nano* **3**, 3015-3022, doi:10.1021/nn900922z (2009).

8 Fung, K. L. Y. *et al.* Accurate EELS background subtraction – an adaptable method in MATLAB. *Ultramicroscopy* **217**, 113052, doi:https://doi.org/10.1016/j.ultramic.2020.113052 (2020).

9 Iakoubovskii, K., Mitsuishi K Fau - Nakayama, Y., Nakayama Y Fau - Furuya, K. & Furuya, K. Thickness measurements with electron energy loss spectroscopy.

10 Shinotsuka, H., Tanuma, S., Powell, C. J. & Penn, D. R. Calculations of electron inelastic mean free paths. X. Data for 41 elemental solids over the 50 eV to 200 keV range with the relativistic full Penn algorithm. *Surface and Interface Analysis* **47**, 871-888, doi:https://doi.org/10.1002/sia.5789 (2015).

11 Keilmann, F. & Hillenbrand, R. Near-field microscopy by elastic light scattering from a tip. *Philos Trans A Math Phys Eng Sci* **362**, 787-805, doi:10.1098/rsta.2003.1347 (2004).

12 Hillenbrand, R. & Keilmann, F. Optical oscillation modes of plasmon particles observed in direct space by phase-contrast near-field microscopy. *Applied Physics B* **73**, 239-243, doi:10.1007/s003400100656 (2014).

13 Ocelic, N., Huber, A. & Hillenbrand, R. Pseudoheterodyne detection for background-free near-field spectroscopy. *Applied Physics Letters* **89**, doi:10.1063/1.2348781 (2006).

14 Al Mohtar, A. *et al.* Generalized lock-in detection for interferometry: application to phase sensitive spectroscopy and near-field nanoscopy. *Opt Express* **22**, 22232-22245, doi:10.1364/OE.22.022232 (2014).

15 Govyadinov, A. A. *et al.* Recovery of Permittivity and Depth from Near-Field Data as a Step toward Infrared Nanotomography. *ACS Nano* **8**, 6911-6921, doi:10.1021/nn5016314 (2014).

16 Shkondin, E. *et al.* Large-scale high aspect ratio Al-doped ZnO nanopillars arrays as anisotropic metamaterials. *Optical Materials Express* **7**, doi:10.1364/ome.7.001606 (2017).

17 Ginn, J. C., Jarecki, R. L., Shaner, E. A. & Davids, P. S. Infrared plasmons on heavily-doped silicon. *Journal of Applied Physics* **110**, 043110, doi:10.1063/1.3626050 (2011).

18 Meng, Y., Anderson, J. R., Hermanson, J. C. & Lapeyre, G. J. Hole plasmon excitations on a p-type GaAs(110) surface. *Physical Review B* **44**, 4040-4043, doi:10.1103/PhysRevB.44.4040 (1991).

19 Poklonski, N. A., Vyrko, S. A., Poklonskaya, O. N., Kovalev, A. I. & Zabrodskii, A. G. Ionization equilibrium at the transition from valence-band to acceptor-band migration of holes in boron-doped diamond. *Journal of Applied Physics* **119**, 245701, doi:10.1063/1.4954281 (2016).